Šprlák M, Han S-C, Featherstone WE (2018) Forward modelling of global gravity fields with 3D density structures and an application to the high-resolution (~ 2km) gravity fields of the Moon. Journal of Geodesy, doi: 10.1007/s00190-017-1098-7.

Forward modelling of global gravity fields with 3D density structures and an application to the high resolution (~2 km) gravity fields of the Moon

M. Šprlák (1), S.-C. Han (1), W.E. Featherstone (2)

(1) School of Engineering, Faculty of Engineering and Built Environment, University of Newcastle, University Drive, Callaghan, NSW 2308, Australia

(2) Department of Spatial Sciences and The Institute for Geoscience Research, Curtin University of Technology, GPO Box U1987, Perth, WA 6845, Australia

Corresponding author: M. Šprlák, Email: michal.sprlak@gmail.com, michal.sprlak@newcastle.edu.au, Tel.: +61 2 4921 8984, Fax: +61 2 4921 6991

ORCIDs: M. Šprlák (0000-0002-3861-7001), S.-C. Han (0000-0003-1810-1670), W.E. Featherstone (0000-0001-9644-4535)

Abstract

Rigorous modelling of the spherical gravitational potential spectra from the volumetric density and geometry of an attracting body is discussed. Firstly, we derive mathematical formulas for the spatial analysis of spherical harmonic coefficients. Secondly, we present a numerically efficient algorithm for rigorous forward modelling. We consider the finite-amplitude topographic modelling methods as special cases, with additional postulates on the volumetric density and geometry. Thirdly, we implement our algorithm in the form of computer programs and test their correctness with respect to the finite-amplitude topography routines. For this purpose, synthetic and realistic numerical experiments, applied to the gravitational field and geometry of the Moon, are performed. We also investigate the optimal choice of input parameters for the finite-amplitude modelling methods. Fourth, we exploit the rigorous forward modelling for the determination of the spherical gravitational potential spectra inferred by lunar crustal models with uniform, laterally variable, radially variable, and spatially (3D) variable bulk density. Also, we analyse these four different crustal models in terms of their spectral characteristics and band-limited radial gravitation. We demonstrate applicability of the rigorous forward modelling using currently available computational resources up to degree and order 2519 of the spherical harmonic expansion, which corresponds to a resolution of ~2.2 km on the surface of the Moon. Computer codes, a user manual and scripts developed for the purposes of this study are publicly available to potential users.

Keywords: bulk density, Newton's integral, spherical harmonic expansion, LOLA, GRAIL

1. Introduction

The gravitational field is one of the fundamental properties of any planetary body. Physical quantities, such as the gravitational potential, components of the gravitational gradient, or components of higher-order gravitational tensors, represent various images of the attracting masses and help indirectly in sensing the inner structure and (sub)-surface processes. Thus, it

forms a tool for understanding surface and interior structures of planetary bodies and for addressing challenging problems in geodesy, geophysics, and planetary sciences.

The gravitational field of any body can be determined by forward modelling. From the mathematical point of view, such modelling is based on Newton's integral for the gravitational potential, while, practically, it exploits information about the geometry and volumetric density distribution of the attracting body.

Forward methods have been used for calculating topographic/terrain effects, striping corrections, or Bouguer gravity anomalies (e.g., Vaníček et al. 1999, Wieczorek 2007, 2015, Vajda et al. 2008, Kuhn et al. 2009, Balmino et al. 2012, Tenzer et al. 2012, Mazarico et al. 2014), testing isostatic hypotheses (e.g., Rummel et al. 1988, Pavlis and Rapp 1990, Grombein et al. 2014), estimating the geoid-to-quasigeoid separation (e.g., Sjöberg 2006, Flury and Rummel 2009, Tenzer et al. 2015, 2016), or determining crustal thickness and Moho depth (e.g., Wieczorek and Phillips 1998, Neumann et al. 2004, James et al. 2013, Wieczorek et al. 2013, Mazarico et al. 2014, Chen and Tenzer 2017).

Forward modelling may be employed in the spatial or spectral domains. In the spatial case, the gravitational potential and its functionals are computed by discretising Newton's integral and its higher-order spatial derivatives by polyhedra or prisms (e.g., Pohánka 1988, Werner and Scheeres 1997, Nagy et al. 2000, D'Urso 2013, Werner 2017), tetrahedra (Casenave et al. 2016), spherical tesseroids (Ku 1977, Asgharzadeh et al. 2007, Heck and Seitz 2007, Wild-Pfeiffer 2008, Li et al. 2011, Uieda et al. 2016), and their ellipsoidal equivalents (Novák and Grafarend 2005, Roussel et al. 2015).

Alternatively, in the spectral domain, spherical (or ellipsoidal) harmonic coefficients of the gravitational potential are evaluated. Various spectral techniques have been developed, such as those based on the rock-equivalent topography (e.g., Lee and Kaula 1967, Balmino et al. 1973, Rummel et al. 1988, Grombein et al. 2016, Kuhn and Hirt 2016), uniform or laterally variable density (e.g., Lachapelle 1976, Balmino 1994, Wieczorek and Phillips 1998, Novák and Grafarend 2006, Wieczorek 2007, Wang and Yang 2013), or multiple density layers (Pavlis and Rapp 1990, Balmino et al. 2012, Tenzer et al. 2016, Rexer et al. 2016, Root et al. 2016).

In this article, we review and discuss the modelling of the gravitational potential spectrum from a 3D spatially variable density and geometry of the attracting body, in this case the Moon. The lunar gravitational field has been improved by Gravity Recovery and Interior Laboratory (GRAIL, Zuber et al. 2013), which motivates us for revealing the detailed inner structure of this body. In contrast to previous methods in the spatial and spectral domains, we do not introduce any unrealistic postulates on the inner structure of the attracting body. Our method corresponds to Newton's integral in the spectral domain and is abbreviated as the Rigorous Forward Modelling (RFM) method. We use a spherical geometry for the Moon, so the resulting spectra are represented by Spherical Harmonic Coefficients (SHCs). The ideas presented in this article can be extended to an ellipsoidal geometry (e.g., for the Earth), but is not discussed here.

We note that RFM is very often considered as computationally too expensive (e.g., Pavlis and Rapp 1990, Wang and Yang 2013). However, our synthetic and real numerical experiments targeted on the lunar gravitational field show that RFM is manageable by using moderately powered computational resources. We verify the correctness of the RFM through several comparisons with respect to the approximate forward modelling techniques by Wieczorek and Phillips (1998) and Wieczorek (2007), herein abbreviated to WP98 and W07. Both methods may also be termed as finite-amplitude methods, as this term is frequently used in the literature. These were intentionally selected as they have become standard procedures in planetary sciences (e.g.,

Neumann et al. 2004, James et al. 2013, Mazarico et al. 2014, Wieczorek 2015). We confirm that the accuracy of these "standard approaches" may be strongly affected by the choice of input parameters (cf. Sun and Sjöberg 2001, Root et al. 2016, Hirt and Kuhn 2017). In contrast, the RFM is more robust and, to simplify and disseminate its exploitation, we make the computer codes, user manual and scripts publicly available to potential users, see Appendix A.

The article is structured as follows. We describe the RFM and the finite-amplitude methods in Section 2. Numerical experiments validating the RFM for the synthetic and realistic scenarios of the gravitational field of the Moon are performed in Section 3. In Section 4, we apply the RFM in comparing four different crustal models of the Moon. Finally, we discuss our main findings in the Conclusions section.

2. Forward modelling of global gravitational fields in the spectral domain

2.1 The RFM method

In this Section, we recapitulate the theoretical foundations for computation of the gravitational potential spectra, i.e., SHCs, provided that the volumetric density and geometry of the attracting body are known (e.g., Kellogg 1929, Heiskanen and Moritz 1967, Torge and Müller 2012, Turcotte and Schubert 2014). We mainly focus on and emphasise the assumptions introduced in these previous mathematical derivations.

Our starting point is the volumetric integral of the mass elements, which allows computation of the gravitational potential V of the attracting body as follows:

$$V(r,\theta,\lambda) = G \iiint \frac{\varrho(r',\theta',\lambda')}{\mathcal{L}(r,\theta,\lambda,r',\theta',\lambda')}\, r'^2 \sin\theta' \mathrm{d}r' \mathrm{d}\theta' \mathrm{d}\lambda' \,. \tag{1}$$

The gravitational potential is calculated at an evaluation point, position of which is defined by spherical geocentric coordinates, i.e., the spherical radius r, spherical co-latitude θ, and spherical longitude λ. The integral runs over an infinitesimal volume (integration) element with spherical coordinates r', θ', λ'. The symbol G in Eq. (1) stands for the universal gravitational constant, ϱ is the volumetric density, and $\mathcal{L}$ is the Euclidean distance between the evaluation point and the integration element.

The key step for transforming the gravitational potential from the spatial domain into the spectral domain is the series representation of the reciprocal Euclidean distance (e.g., Heiskanen and Moritz 1967, p. 58):

$$\begin{aligned} \frac{1}{\mathcal{L}(r,\theta,\lambda,r',\theta',\lambda')} &= \frac{1}{r'} \sum_{l=0}^{\infty} \left(\frac{r'}{r}\right)^{l+1} P_l(\cos\psi) \\ &= \frac{1}{r'} \sum_{l=0}^{\infty} \sum_{m=0}^{l} \left(\frac{r'}{r}\right)^{l+1} \frac{1}{2l+1} [\bar{P}_{lm}(\cos\theta) \cos m\lambda\, \bar{P}_{lm}(\cos\theta') \cos m\lambda' \\ &\qquad + \bar{P}_{lm}(\cos\theta) \sin m\lambda\, \bar{P}_{lm}(\cos\theta') \sin m\lambda' \,]. \end{aligned} \tag{2}$$

The expression after the first equality sign represents the infinite series in terms of un-normalised Legendre polynomials P_l of degree l. These are functions of the spherical distance ψ between the evaluation point and the integration element, calculated from θ, λ and θ', λ' using spherical trigonometry. The second series makes use of the addition theorem (e.g., Heiskanen and Moritz

1967, Eq. 1-82'), which decomposes the un-normalised Legendre polynomials into the sum of the products of 4π fully-normalised spherical harmonics:

$$\bar{Y}_{lm}(\theta,\lambda) = \bar{P}_{lm}(\cos\theta)\begin{Bmatrix}\cos m\lambda \\ \sin m\lambda\end{Bmatrix}, \tag{3}$$

with $\bar{P}_{lm}$ being the fully-normalised associated Legendre functions of the first kind of degree l and order m. Both infinite series in Eq. (2) converge uniformly for any evaluation point $r > r'$ (e.g., Heiskanen and Moritz 1967, p. 33). Convergence is also guaranteed if $r = r'$ unless the evaluation point and the integration element become identical (Arfken and Weber 2005, p. 743). A singularity occurs in this case and both series diverge. Importantly, and as we will demonstrate later, r must be external to the gravitating masses.

We now substitute Eq. (2) into the Newton integral of Eq. (1). With the assumption of the uniform convergence, which is valid for any $r > r'$, we change the order of the double summation and the volume integration. These operations lead to the spectral representation of the gravitational potential in the form:

$$\begin{aligned} V(r,\theta,\lambda) &= G\sum_{l=0}^{\infty}\sum_{m=0}^{l}\left(\frac{1}{r}\right)^{l+1}\frac{1}{2l+1} \\ &\times\Big\{\bar{P}_{lm}(\cos\theta)\cos m\lambda\iiint \varrho(r',\theta',\lambda')\,\bar{P}_{lm}(\cos\theta')\cos m\lambda'\,r'^{l+2}\sin\theta'\mathrm{d}r'\mathrm{d}\theta'\mathrm{d}\lambda' \\ &+\bar{P}_{lm}(\cos\theta)\sin m\lambda\iiint \varrho(r',\theta',\lambda')\,\bar{P}_{lm}(\cos\theta')\sin m\lambda'\,r'^{l+2}\sin\theta'\mathrm{d}r'\mathrm{d}\theta'\mathrm{d}\lambda'\Big\}. \end{aligned} \tag{4}$$

To extract the fully-normalised SHCs $\bar{C}_{lm}, \bar{S}_{lm}$ from Eq. (4), we use the corresponding expansion of the external gravitational potential:

$$V(r,\theta,\lambda) = \frac{GM}{R}\sum_{l=0}^{\infty}\sum_{m=0}^{l}\left(\frac{R}{r}\right)^{l+1}\left[\bar{C}_{lm}\,\bar{P}_{lm}(\cos\theta)\cos m\lambda + \bar{S}_{lm}\,\bar{P}_{lm}(\cos\theta)\sin m\lambda\right], \tag{5}$$

where M is the total mass of the attracting body and R is the radius of the Brillouin sphere, which is any sphere fully enclosing all gravitating masses of the body (e.g., Sansò and Sideris 2013, Sect. 3.2). Equation (5) is the solution of Laplace's equation in spherical geocentric coordinates. It requires that the gravitational potential is harmonic, which is true only outside the gravitating masses. In our study of the Moon, we do not need to consider an atmosphere. Convergence of Eq. (4) is always guaranteed on the surface and outside the Brillouin sphere (e.g., Jekeli 1981, Moritz 1989, Chapters 6 and 7).

Comparing Eqs. (4) and (5), and taking $R = r > r'$, the expression for evaluation of the SHCs reads:

$$\left.\begin{matrix}\bar{C}_{lm} \\ \bar{S}_{lm}\end{matrix}\right\} = \frac{1}{R^l\,M\,(2n+1)}\iiint \varrho(r',\theta',\lambda')\,\bar{P}_{lm}(\cos\theta')\left\{\begin{matrix}\cos m\lambda' \\ \sin m\lambda'\end{matrix}\right\}r'^{l+2}\sin\theta'\mathrm{d}r'\mathrm{d}\theta'\mathrm{d}\lambda'\,. \tag{6}$$

Except for the density ϱ, information about the geometry of the body has to be known. This is required by the limits of the volume integral and is available in the form of Digital Elevation Models (DEMs).

2.2 Practical implementation

Equation (6) is a theoretical prescription for transforming the volumetric density and geometry of the body into SHCs. We now describe an efficient and accurate algorithm for computation of the spherical gravitational potential spectra by discretising the integral and using the discrete Fourier transform.

We start by discretising the volume of the attracting body into spherical tesseroids. A tesseroid is defined by indices i, j, k and bounded by spherical coordinates $r'_k \le r' < r'_k + \Delta r'$, $\theta'_i \le \theta' < \theta'_i + \Delta\theta', \lambda'_j \le \lambda' < \lambda'_j + \Delta\lambda'$, where $\Delta r', \Delta\theta'$, and $\Delta\lambda'$ are the respective discretisation steps. The volumetric density is assumed to be constant inside each tesseroid and is represented by its mean value $\bar{\varrho}(r'_k, \theta'_i, \lambda'_j)$, but this value can be different for each tesseroid, thus allowing for practical implementation of variable densities. The discretised version of Eq. (6) then reads:

$$\left.\begin{matrix}\bar{C}_{lm}\\ \bar{S}_{lm}\end{matrix}\right\} = \frac{1}{R^l\, M\, (2l+1)} \sum_{i,j,k} \bar{\varrho}(r'_k, \theta'_i, \lambda'_j) \times \int_{\theta'_i}^{\theta'_i+\Delta\theta'} \bar{P}_{lm}(\cos\theta') \sin\theta' \, \mathrm{d}\theta' \int_{\lambda'_j}^{\lambda'_j+\Delta\lambda'} \left\{\begin{matrix}\cos m\lambda'\\ \sin m\lambda'\end{matrix}\right\} \mathrm{d}\lambda' \int_{r'_k}^{r'_k+\Delta r'} r'^{l+2}\, \mathrm{d}r'. \tag{7}$$

The volume integral of Eq. (6) has now been transferred into the triple summation $\sum_{i,j,k} = \sum_i \sum_j \sum_k$ over all tesseroids within the attracting body. The three integrals with respect to the spherical coordinates of the integration element appear in Eq. (7). These are the integral mean values of the corresponding functions over the tesseroid with indices i, j, k.

By exploiting rules of integral calculus, the integral over the spherical radius multiplied by the term $1/R^l$ can be expressed analytically and exactly as:

$$\frac{1}{R^l} \int_{r'_k}^{r'_k+\Delta r'} r'^{l+2}\, \mathrm{d}r' = \frac{R^3}{l+3}\left[\left(\frac{r'_k + \Delta r'}{R}\right)^{l+3} - \left(\frac{r'_k}{R}\right)^{l+3}\right]. \tag{8}$$

Also, the analytical form of the integral over the spherical longitude exists. Together with identities for the trigonometric functions and by considering $\lambda'_j = j\Delta\lambda'$, we obtain:

$$\int_{\lambda'_j}^{\lambda'_j+\Delta\lambda'} \left\{\begin{matrix}\cos m\lambda'\\ \sin m\lambda'\end{matrix}\right\} \mathrm{d}\lambda' = \left\{\begin{matrix} A_m \cos(mj\Delta\lambda') + B_m \sin(mj\Delta\lambda')\\ -B_m \cos(mj\Delta\lambda') + A_m \sin(mj\Delta\lambda')\end{matrix}\right. . \tag{9}$$

The auxiliary coefficients A_m, B_m are:

$$A_m = \begin{cases} \Delta\lambda', & m = 0, \\ \dfrac{\sin(m\Delta\lambda')}{m}, & \forall m \geq 1, \end{cases} \qquad B_m = \begin{cases} 0, & m = 0, \\ \dfrac{\cos(m\Delta\lambda') - 1}{m}, & \forall m \geq 1. \end{cases} \tag{10}$$

The integral over the spherical co-latitude in Eq. (7) is non-trivial. However, it can be computed by recursive formulas (e.g., Paul 1978, Gerstl 1980, Gleason 1985, Fukushima 2012a). The integrals of the associated Legendre functions of the first kind will be abbreviated by:

$$\int_{\theta_i'}^{\theta_i'+\Delta\theta'} \bar{P}_{lm}(\cos\theta') \sin\theta' \, \mathrm{d}\theta' = \overline{IP}_{lm,i}. \tag{11}$$

Considering the expressions of Eqs. (8)-(11), the SHCs can be calculated as:

$$\begin{Bmatrix} \bar{C}_{lm} \\ \bar{S}_{lm} \end{Bmatrix} = \frac{R^3}{M\,(2l+1)(l+3)} \sum_{i,j,k} \bar{\varrho}\left(r_k', \theta_i', \lambda_j'\right) \overline{IP}_{lm,i} \begin{Bmatrix} A_m \cos(mj\Delta\lambda') + B_m \sin(mj\Delta\lambda') \\ -B_m \cos(mj\Delta\lambda') + A_m \sin(mj\Delta\lambda') \end{Bmatrix} \times \left[\left(\frac{r_k' + \Delta r'}{R} \right)^{l+3} - \left(\frac{r_k'}{R} \right)^{l+3} \right]. \tag{12}$$

Equation (12) consists of the three summations over the tesseroid indices i, j, k that may be computationally expensive for small tesseroids. However, the evaluation can significantly be accelerated by exploiting the 1D discrete Fourier transform (cf. Haagmans et al. 1993) with respect to j (i.e., the spherical longitude index). For this purpose, we firstly introduce the coefficients:

$$d_{l,ij} = \sum_k \bar{\varrho}\left(r_k', \theta_i', \lambda_j'\right) \left[\left(\frac{r_k' + \Delta r'}{R} \right)^{l+3} - \left(\frac{r_k'}{R} \right)^{l+3} \right]. \tag{13}$$

These depend on the spherical harmonic degree l and the tesseroid position in the direction of the spherical co-latitude and spherical longitude, i.e., the indices i and j. Once the coefficients $d_{l,ij}$ are computed, we can obtain its Fourier coefficients as follows:

$$\begin{Bmatrix} X_{lm,i} \\ Z_{lm,i} \end{Bmatrix} = \sum_j d_{l,ij} \begin{Bmatrix} \cos(mj\Delta\lambda) \\ \sin(mj\Delta\lambda) \end{Bmatrix} = \begin{cases} \Re\left[\mathcal{F}\left(d_{l,ij}\right)_m\right] \\ \Im\left[\mathcal{F}\left(d_{l,ij}\right)_m\right] \end{cases}. \tag{14}$$

Equation (14) reveals that $X_{lm,i}$ and $Z_{lm,i}$ are the Fourier coefficients of frequency m for the summation of the uniform samples of $d_{l,ij}$ over the spherical longitude index j. These can efficiently be calculated by the 1D discrete Fourier transform as they represent its real $\Re$ and imaginary $\Im$ parts.

Taking into account Eqs. (13) and (14), we can calculate the SHCs based on the formula:

$$\left.\begin{matrix}\bar{C}_{lm}\\ \bar{S}_{lm}\end{matrix}\right\} = \frac{R^3}{M(2l+1)(l+3)} \sum_i \overline{IP}_{lm,i} \left\{\begin{matrix} A_m\, X_{lm,i} + B_m\, Z_{lm,i} \\ -B_m\, X_{lm,i} + A_m\, Z_{lm,i}\end{matrix}\right\}. \tag{15}$$

From the numerical point of view, the accuracy of such a computation depends on the discretisation size of the tesseroids. The discretisation must correspond at least to the maximum degree and order (d/o) of the SHCs. Computation of the fully-normalised associated Legendre functions of the first kind and their tesseroid mean values (see Eq. (11)) may also be subject to the numerical problems (IEEE underflow or overflow) for a high degree analysis, e.g., if $l, m > 1800$. The numerical problems can, however, be avoided by implementing stable recursion algorithms (e.g., Holmes and Featherstone 2002) or extended-precision arithmetic (e.g., Fukushima 2012a, b).

2.3 Comparison with other methods (WP98 and W07)

The method of W07 is based on the same initial points and assumptions as already discussed in Section 2.1. This approach can be obtained from Eq. (6) by introducing two additional postulates: 1) the density within the attracting body is constant in the radial direction, i.e., it is only a function of the spherical co-latitude and spherical longitude, 2) split the spherical radius of the integration element as $r' = D + H$, where H is the topographic height, which depends on the spherical co-latitude and spherical longitude. The symbol D stands for the constant radius and defines an auxiliary sphere that is termed herein as the topographic sphere. In the context of convergence of the spectrum, we highlight here that this topographic sphere may be partly inside the gravitating masses.

By considering the binomial theorem for the $(l+2)$-th power of $D + H$, see Eq. (6), the SHCs become:

$$\left.\begin{matrix}\bar{C}_{lm}\\ \bar{S}_{lm}\end{matrix}\right\} = \frac{4\pi\, D^3}{M\,(2l+1)\,(l+3)} \sum_{n=1}^{l+3} \frac{\prod_{j=1}^{n}(l+4-j)}{D^n\, n!} \left\{\begin{matrix}\overline{\varrho HC}_{lm}^{n}\\ \overline{\varrho HS}_{lm}^{n}\end{matrix}\right\}, \tag{16}$$

where the spectra for the n-th power of the topographic heights multiplied by the laterally variable density is defined by the formula:

$$\left.\begin{matrix}\overline{\varrho HC}_{lm}^{n}\\ \overline{\varrho HS}_{lm}^{n}\end{matrix}\right\} = \frac{1}{4\pi} \iint \varrho(\theta', \lambda')\, H^n(\theta', \lambda')\, \bar{P}_{lm}(\cos\theta') \left\{\begin{matrix}\cos m\lambda' \\ \sin m\lambda'\end{matrix}\right\} \sin\theta' \mathrm{d}\theta' \mathrm{d}\lambda'. \tag{17}$$

If a constant density is assumed within the attracting body (as in WP98), Eq. (17) simplifies to:

$$\left.\begin{matrix}\bar{C}_{lm}\\ \bar{S}_{lm}\end{matrix}\right\} = \frac{4\pi\, \varrho\, D^3}{M\,(2l+1)\,(l+3)} \sum_{n=1}^{l+3} \frac{\prod_{j=1}^{n}(l+4-j)}{D^n\, n!} \left\{\begin{matrix}\overline{HC}_{lm}^{n}\\ \overline{HS}_{lm}^{n}\end{matrix}\right\}, \tag{18}$$

with the spectra for the n-th power of the topographic heights in the form:

$$\left.\begin{matrix}\overline{HC}_{lm}^{n}\\ \overline{HS}_{lm}^{n}\end{matrix}\right\} = \frac{1}{4\pi}\iint H^{n}(\theta',\lambda')\,\bar{P}_{lm}(\cos\theta')\left\{\begin{matrix}\cos m\lambda'\\ \sin m\lambda'\end{matrix}\right\}\sin\theta'\mathrm{d}\theta'\mathrm{d}\lambda' . \tag{19}$$

From Eq. (18), the gravitational potential spectrum is based purely on the geometric properties of the attracting body. The bulk density of the body merely represents a scaling factor to the gravitational potential as it now resides outside the integration/summation. We contend that this is a key limitation of the finite-amplitude (WP98 and W07) methods if one wishes to include variable density information in forward modelling of planetary gravitational fields.

Several items must be considered when exploiting Eqs. (16)-(17) or (18)-(19) in practical calculations. First, the SHCs of Eqs. (16) and (18) refer to the topographic sphere of radius D. The convergence of the corresponding gravitational potential is guaranteed only on or above the Brillouin sphere. When the topographic sphere is located inside the attracting body, as is often selected in practical calculations (e.g., Wieczorek 2015), the gravitational potential spectrum must be continued upward to its Brillouin counterpart. Only in this way can one obtain truly realistic gravitational field that strictly fulfils Laplace's equation, i.e., harmonicity.

Secondly, the choice of the topographic sphere directly affects the topographic SHCs from Eqs. (17) and (19), and therefore also the number of significant terms in the summation over the power (index) n in Eqs. (16) and (18). For example, when the topographic sphere completely encloses the topography, the spectrum for the n-th power of the topographic heights may become more pronounced as compared to the one for the mean topographic sphere. This is because the topographic heights possess large values and are of the same sign for the enclosing topographic sphere, while the topographic heights alternate around zero for the mean topographic sphere.

Thirdly, the maximum value of the summation index n in Eqs. (16) and (18), herein referred to as the maximum power of the topographic expansion, goes theoretically up to $l+3$. In practical calculations, the summation over the power (index) n is truncated at a much lower value than $l+3$. However, the maximum power of the topographic expansion must be properly selected as it influences the accuracy of the gravitational potential SHCs $\bar{C}_{lm}, \bar{S}_{lm}$. For instance, a criterion may be chosen based on the accuracy of available gravitational models, as both actual gravitational and topography (crustal) implied fields are very often assessed by other measures such as correlation or admittance. A general formula for determining the maximum power of the topographic expansion does not exist and its value should be estimated empirically for any planetary body (e.g., Sun and Sjöberg 2001, Wieczorek 2015, Rexer et al. 2016).

Fourthly, grids of topographic heights (DEMs) are usually exploited for the computation of the topographic SHCs by Eqs. (17) and (19). The grid discretisation should be fine enough to avoid aliasing when higher powers of the topographic heights are analysed (Hirt and Kuhn 2014). Given the maximum d/o of the topographic SHCs, the discretisation size should decrease inverse-proportionally to the power n of the topographic heights. This is not feasible for high d/o spherical harmonic expansions. In practice, DEMs are padded with zero values. Alternatively, DEMs are discretised with steps $\Delta\theta'$ and $\Delta\lambda'$ that correspond to twice the maximum d/o of the harmonic expansion (e.g., Wieczorek et al. 2015).

3. Numerical results

We developed a FORTRAN program (Appendix A) employing the RFM based on Eq. (15). The program makes use of the scaling algorithm by Holmes and Featherstone (2002) that allows for computing the integrals of the associated Legendre functions of the first kind, see Eq. (11), up to

d/o 2700. The 1D discrete Fourier transform is performed by the FORTRAN routine FFTCC (Boisvert et al. 1984).

We compared the results with the modelling approaches by WP98 and W07 implemented in the FORTRAN routines CilmPlus and CilmPlusRhoH, which are functions within the software suite SHTOOLS (Wieczorek et al. 2015). These also exploit the stabilisation procedure by Holmes and Featherstone (2002). Several spherical harmonic analysis methods are available within SHTOOLS, among which we opted for the one by Driscoll and Healy (1994).

In this Section, we focus on testing the three modelling methods (RFM, WP98, and W07) for synthetic/simulated and realistic gravitational fields of the Moon. In this way, we confirm correctness of the RFM algorithm and demonstrate its applicability. Moreover, we point out the numerical restrictions for the finite-amplitude methods. In Section 4, we further compute several gravitational models of the Moon exploring different crustal density structures. Therefore, geometric and physical parameters of the numerical experiments were chosen such that they suit this planetary body, but they can be applied elsewhere.

All gravitational potential spectra were calculated up to d/o 2519. Such a spherical harmonic expansion corresponds to an angular resolution of 1/14° at the lunar equator (or the resolution of ~2.2 km on the surface of the Moon). A DEM with the corresponding sampling (or its resampled analogues) was used by the RFM. The algorithm by Driscoll and Healy (1994) guarantees accurate analysis when the angular sampling is at least twice as fine as the one conforming with the maximum spherical harmonic d/o. Therefore, we exploited DEM grids discretised with steps of at most $\Delta\theta' = \Delta\lambda' = 1/28°$ when modelling the gravitational potential spectra by the finite-amplitude methods. We also note that the discretisation in the radial direction for the RFM algorithm was kept constant with the size of $\Delta r' = 1$ km.

We performed the numerical experiments on a desktop computer with 32 GB of RAM and a processor with eight cores, each of frequency 3.4 GHz, in a Linux 64-bit operating system, while exploiting only one core at a program runtime.

3.1 Gravitation of a spherical shell

We start the numerical experiments for a simple synthetic case of the spherical shell with a constant density ϱ. The spherical harmonic spectra in such case can be solved analytically and is defined by the formula:

$$\left.\begin{matrix}\bar{C}_{nm}\\ \bar{S}_{nm}\end{matrix}\right\} = \begin{cases}\dfrac{4\pi\varrho(R_2^3 - R_1^3)}{3M}\,\delta_{n,0}\,\delta_{m,0}\,, \\ 0\end{cases} \tag{20}$$

where $\delta_{i,j}$ is the Kronecker delta, R_1, R_2 are the radii of the lower and upper spheres forming the shell such that $R_1 \leq R_2$. Except for $\bar{C}_{00}$, the SHCs are zero that served as a benchmark for assessing the accuracy of the three modelling methods (RFM, WP98, and W07).

For this purpose, we firstly generated the theoretically exact spectra from Eq. (20). We opted for the constant density value $\varrho = 2550\ \mathrm{kg/m^3}$, radii of the lower and upper spheres $R_1 = 1740$ km and $R_2 = 1750$ km, and the lunar mass $M = 7.3458996 \times 10^{22}$ kg. The radii of the upper sphere $R_2 = 1765$ km and 1790 km were also tested and did not affect conclusions from this numerical experiment.

To be consistent with the theoretical spectra of Eq. (20), the same bulk density values, either as a single value or as a grid file, and of the mass were taken into account. For the finite-

amplitude methods, the radius of the topographic sphere was set to $D = R_2$, see Eqs. (16) and (18). We generated a grid of the constant topographic height $H = -10$ km so as to be in agreement with the choice of the topographic sphere D and the 10 km thickness of the spherical shell, see Eqs. (17) and (19). The synthetic topography was discretised with the steps $\Delta\theta' = \Delta\lambda' = 1/28°$.

The performance of the routines CilmPlus (WP98) and CilmPlusRhoH (W07) was tested for the maximum powers of the topographic expansion $n_{max} = 1, 10, \text{and } 20$. In the case of the RFM, we exploited the same global grid of the constant topographic height as we chose the radius of the Brillouin sphere $R = R_2 = 1750$ km, see Eq. (15). Unlike WP98 and W07, no other parameters were required by the RFM.

Finally, the theoretical SHCs of Eq. (20) were subtracted from those obtained by the three modelling approaches. The coefficient differences were exploited for computing the square-root of degree variances and depicted in Fig. 1.

Preferred location of Fig. 1

The black curve in Fig. 1 shows the relative performance of the RFM. The accuracy is 10^{-16} for low d/o spherical harmonics and decreases to less than 10^{-21} by increasing d/o of the expansion to 2519. We suspect that the degree-dependent improvement of accuracy is mainly caused by the decreasing magnitudes of the fully normalised associated Legendre functions of the first kind (e.g., Holmes and Featherstone 2002). We note that the only non-zero SHC is $\bar{C}_{00}$, which was determined with the relative accuracy of 10^{-12}.

Similar performance is also revealed for the approach by WP98. Moreover, the red, blue and green curves in Fig. 1 indicate even higher accuracy for the lower powers of the topographic expansion. This can be explained by fewer mathematical operations necessary for the numerical calculations. However, in a more realistic scenario, such as the one in Section 3.2, higher-power topographic expansions are necessary to achieve the required precision of the modelling approach (e.g., Sun and Sjöberg 2001, Wieczorek 2015, Rexer et al. 2016). Almost identical results were obtained by the routine CilmPlusRhoH, which implements the procedure by W07 and also for the finer resolution of the DEM grid with a spacing of 1/56° (corresponding to a resolution of ~0.5 km on the surface of the Moon). These additional results are not presented in Fig. 1 as the conclusions remain the same.

Overall, the synthetic test proves very good accuracy of the three algorithms, even below the machine epsilon of double precision arithmetic. We have not identified any systematic errors, either for high spherical harmonic degrees and orders (ds/os), high powers of topographic expansions or very fine discretisation of the synthetic DEM grid.

3.2 Gravitation from the actual lunar topography

We now focus on the comparison of the three forward modelling approaches in a more realistic scenario on the Moon. The lunar surface geometry is provided by the Lunar Orbiter Laser Altimeter (LOLA, Smith et al. 2010) topography. We used the gridded data record in the Principal Axis coordinate system. This ensures a consistent coordinate system with the global gravitational models of the Moon, such as from GRAIL. The dataset consists of globally interpolated LOLA heights H_{LOLA} with equiangular sampling of 1/64°. These are referenced to the mean sphere of radius $R_{LOLA} = 1737.4$ km, see (http://pds-geosciences.wustl.edu/lro/lro-l-lola-3-rdr-v1/lrolol_1xxx/data/lola_gdr/cylindrical/pa/).

The above LOLA topography was smoothed such that the new DEM grid had equiangular sampling of 1/14°, corresponding to spherical harmonic d/o 2519. For this purpose, we exploited the program *blockmean*, which is available within the Generic Mapping Tools (GMT, Wessel et al. 2013) suite to compute the mean topographic heights over the elements required for the numerical integration. Two finer grids, discretised with steps $\Delta\theta' = \Delta\lambda' = 1/28°$ and 1/56°, were also employed in our numerical experiments. These were obtained by dividing the integration elements of size 1/14°, within which the topographic heights were preserved. Thus, the finest spatial resolution of all LOLA topography grids is always 1/14°.

The calculated gravitational fields were inferred by the surplus or deficit lunar topographic masses above or below the sphere of radius $R_{LOLA} = 1737.4$ km. However, we emphasize that all gravitational potential spectra were referred to the Brillouin sphere of radius $R = R_{LOLA} + max(H_{LOLA}) = 1748.2$ km. Thus, continuation of SHC was performed if the SHCs were initially referred to another spherical surface, e.g., the topographic sphere of radius $D < R$.

Preferred location of Fig. 2

The necessity for the Brillouin sphere is also justified with the support of Fig. 2. Convergence of the gravitational potential spectra inferred by the topographic masses of the Moon is guaranteed only for the Brillouin radius $R = R_{LOLA} + max(H_{LOLA}) = 1748.2$ km (green curve). For the other three non-Brillouin spheres of radii $R = R_{LOLA} + min(H_{LOLA}) = 1728.2$ km, $R = R_{LOLA} = 1737.4$ km, and $R = 1738.0$ km (red, blue and black curves, respectively), the powers of the gravitational spectra amplify with increasing d/o. We note that the selection of the Brillouin sphere conforms with Hirt and Kuhn (2017), who also pointed out this issue by investigating the convergence of the gravitational potential spectra inferred by the lunar topography.

In addition, we emphasise the divergence of the gravitational spectra above d/o ~800 for $R = 1738.0$ km. As this is the preferred reference radius of GRAIL gravitational field models (Konopliv et al. 2013, 2014, Lemoine et al. 2013, 2014), their gravitational spectra should also experience the diverging behaviour observed in Fig. 2. However, high d/o SHCs of GRAIL-derived models are very often constrained by decreasing power laws (e.g., Kaula 1966), which eventually leads to undesired smoothing.

3.2.1 Optimal selection of input parameters in WP98 and W07

Here, we investigate the numerical restrictions in WP98 and W07. Specifically, we study how the computation of the gravitational spectra is influenced by: 1) the maximum power of the topographic expansion n_{max} and 2) the radius of the topographic sphere D. The effect of DEM grid sampling is partially addressed in Section 3.2.2. We considered the three radii of the topographic sphere: 1) $D = R_{LOLA} + min(H_{LOLA}) = 1728.2$ km, 2) $D = R_{LOLA} = 1737.4$ km, and 3) $D = R_{LOLA} + max(H_{LOLA}) = 1748.2$ km. Similar to the example of the spherical shell (Section 3.1), we also tested three different powers of the topographic expansion, i.e., $n_{max} = 1, 10, \text{and } 20$.

The finite-amplitude modelling methods differ only by the postulate about the bulk density. We used $\varrho = 2550$ kg/m^3 for WP98 and a laterally variable density for W07. The lateral density grid with the same equiangular sampling as the LOLA topography was obtained in two steps: 1) by synthesising the grain density from the SHCs provided by Wieczorek et al. (2013) up to d/o 310, 2) scaling the grain density values such that their global average equals to

2550 kg/m^3. The scaling transformed the grain density into its bulk counterpart. The scaling factor applied was ~0.88. This corresponds to an average porosity of ~12%, which appears to be a realistic value for the upper part of the lunar crust (e.g., Wieczorek et al. 2013, Han et al. 2014).

For the purpose of this numerical experiment, one could opt for other density behaviours within the lunar topographic masses. However, we intentionally chose the realistic density values as these were also exploited in comparing different crustal models of the Moon in Section 4.

Preferred location of Fig. 3

The square root of the degree variances for the gravitational potential spectra are illustrated in Fig. 3. These were obtained by the method of WP98 for different values of D and n_{max}. Intuitively, all of the curves should be identical or converge to the solid black curve. However, Fig. 3 reveals a fair agreement with the solid black curve only for some of the spectra within a limited spherical harmonic band. On the other hand, we observe completely diverging spectra depending on the choice of the input parameters.

The radius of the topographic sphere D significantly affects the computation of the SHCs. The blue curves in Fig. 3 show that the total power is overestimated and may be even completely unrealistic after d/o 450 or 800 when taking the maximum radius of the topographic sphere $D = 1748.2$ km. On the other hand, the spectra are underestimated when considering $D = 1728.2$ km, i.e., the minimum radius, as the behaviour of the red curves in Fig. 3 indicates. By selecting the radius D such that it represents approximately the mean sphere, i.e., $D = 1737.4$ km (black curves), shows the most rapid convergence.

Another parameter affecting the performance of WP98 method is the maximum power of the topographic expansion n_{max}. It is seen in Fig. 3 that the low values, e.g., $n_{max} = 1$, do not provide realistic spectra. Figure 3 also suggests that the higher power topographic expansions are required for $D = 1728.2$ km and 1748.2 km as compared to $D = 1737.4$ km. This again favours the selection of the mean sphere in practical computations.

Preferred location of Fig. 4

Figure 4 illustrates the square root of degree variances for the individual terms of selected power (index) n in Eq. (18). This is different from the total (cumulative) effect obtained by summing up all terms with powers (indices) between 1 – n_{max} in Eq. (18) and presented in Fig. 3. It can be seen in Fig. 4 that low d/o SHCs originate from the low-power topographic terms. In contrast, the high-power topographic terms significantly contribute to the high d/o part of the gravitational potential spectra that proves divergence of Eq. (18).

For $n = 1$, selection of the topographic sphere only changes the SHC $\bar{C}_{00}$, while the other coefficients are preserved. In such a case, the spectra are identical for all $l \geq 1$, as illustrated by the dotted black curve in Fig. 4. We note that the distinct powers of the gravitational spectra for $n_{max} = 1$ in Fig. 3 are caused by subsequent upward continuation of the SHCs from the different topographic spheres to the Brillouin sphere.

For high-power terms of the topographic expansion, the SHCs vary based on the choice of the topographic sphere. Considering $D = 1748.2$ km (blue curves in Fig. 4), the corresponding topographic heights have the same sign and possess large values. By analysing such topographic

heights, we observe that the individual terms become more significant with the increasing power of topography n. Consequently, we can see diverging gravitational spectra in Figs. 3 and 4.

For the topographic sphere of radius $D = 1728.2$ km, the power of the individual terms is close to those of $D = 1748.2$ km, as the topographic heights have again only the same sign and large values. However, the observed underestimation in Fig. 3 is a result of upward continuation from the topographic sphere onto its Brillouin counterpart. The topographic sphere of radius $D = 1737.4$ km causes the topographic heights to be of alternating sign and smaller magnitudes. The resulting power of the gravitational spectra is therefore reduced and converges, as observed in Figs. 3 and 4.

Hirt and Kuhn (2017) performed an investigation of the WP98 method and its performance for the Moon. They studied how the spatial resolution of the lunar topography affects the gravitational potential spectra. Considering only one radius of the topographic sphere in the spectral analyses, i.e., $D = 1738.0$ km, they detected diverging spectra for the finest topographic surfaces. In addition, they compared gravity values obtained by the Newtonian integration and the WP98 method in the spatial domain. Their analyses indicated that gravity values were strongly influenced by the choice of the Brillouin sphere. However, the numerical restrictions of WP98 method investigated in this section are different from and complementary to those addressed by Hirt and Kuhn (2017).

We note that the numerical experiments (not presented here) with the routine CilmPlusRhoH exploiting W07 led to identical conclusions as presented above.

3.2.2 Numerical comparison of RFM and WP98

Here, we compare RFM and the approach by WP98. The RFM algorithm was tested with the assumption of a constant density $\varrho = 2550$ kg/m^3 and discretisation sizes of the LOLA topography grid of $\Delta\theta' = \Delta\lambda' = 1/14°$, 1/28°, and 1/56°. For the forward modelling by WP98, we considered the maximum power of the topographic expansion n_{max}= 20, the radius of the topographic sphere $D = 1737.4$ km, and the LOLA topography grid with equiangular samplings of 1/28° and 1/56°. (Recall that all LOLA topography grids possess the finest spatial resolution of 1/14°). The finer grids represent only geometric refinements to investigate discretisation errors for RFM and quantify the aliasing effect for the WP98 method.

Preferred location of Fig. 5

The comparison between RFM and WP98 is illustrated in Fig. 5. However, in contrast to the synthetic case in Section 3.1, the true gravitational potential spectrum is not known for this scenario. Nevertheless, we selected the true (reference) gravitational potential spectrum as obtained by the RFM with the LOLA topography grid discretised with the steps $\Delta\theta' = \Delta\lambda' = 1/14°$ (black curve in Fig 5). We were justified to do so as the RFM approach is based on the least number of postulates and is completely free of the numerical issues present in the finite-amplitude methods.

Ultimately, the RFM algorithm is affected by discretisation errors, i.e., the uncertainties due to the different size of tesseroids. When refining the sampling of LOLA topography to 1/28° (green curve in Fig. 5), the differences of the gravitational spectra are at least 12 orders of magnitude smaller than the reference signal. Identical behaviour was found for the LOLA topography grid with equiangular sampling of 1/56°. Thus, the discretisation errors for the RFM are negligible.

The gravitational spectra of RFM and WP98 differ by approximately two orders of magnitude for low ds/os, while the distinctions are more pronounced by increasing the harmonic d/o (red curve in Fig. 5). Based on the previous numerical experiments (Section 3.2.1), the radius of the topographic sphere $D = 1737.4$ km is the optimal one and did not further improve the performance of WP98. The resulting gravitational potential spectra was neither affected by larger value of the maximum power of the topographic expansion n_{max}= 25.

However, the differences between RFM and WP98 decreased when we exploited the finest LOLA grid discretised at 1/56° (blue curve in Fig 5). This suggests that the topographic grid sampling, and thus also the aliasing effect originating from analysis of higher powers of the topographic heights, may still influence the SHCs. The effect of the grid sampling is below the power of the signal and becomes important only when the other parameters, i.e., the radius of the topographic sphere D and the maximum topography power n_{max}, are selected properly. Further refinements of the topography grid are not feasible for practical reasons, e.g., due to significant memory requirements or increasing computational effort. We emphasise that our observations for the finite-amplitude approaches hold true for the spherical harmonic analysis algorithm by Driscoll and Healy (1994) and results may be different when alternative analysis methods are applied.

We also acknowledge that the differences between RFM and WP98 method presented in Fig. 5 may also come from distinct calculation of spherical harmonics. The RFM algorithm computes the mean values of the spherical harmonics at the angular centres of tesseroids. The routine CilmPlus calculates point values of spherical harmonics at the corner points of discretised spherical surface. The two spherical harmonic calculations are not further investigated as we suppose these may be negligible for high-resolution grids such as those exploited in this article.

We also compared the RFM with W07 using the laterally variable density (not presented here), and did not find any different conclusions.

4. Comparison of gravitational potential models from variable densities with GRAIL observations

We considered four crustal models that differ by the assumptions of the bulk density, comprising: 1) constant, 2) laterally variable, 3) radially variable, and 4) spatially variable in 3D. We chose the base of the lunar crust to be at a radius of 1680 km. The upper boundary of the crustal models was represented by the LOLA topography grid with the equiangular sampling of 1/14°. Based on the previous experiments, the four gravitational potential spectra were computed up to d/o 2519, referred to the Brillouin sphere of radius $R = R_{LOLA} + max(H_{LOLA}) =$ 1748.2 km, and the radial discretisation of tesseroids was $\Delta r' = 1$ km.

For the constant density model, we assigned the density $\varrho = 2550$ kg/m^3 to all tesseroids. The second crustal model included the 2D density grid introduced in Section 3.2. The third crustal model was based on the exponential compaction model of the density distribution in the radial direction defined as (e.g., Athy 1930, Audet and Fowler 1992):

$$\varrho(r) = \varrho_0 \left\{ 1 - \phi_1 \, exp\left[-c \frac{P(r)}{P_c} \right] \right\}, \tag{21}$$

where $c \approx 6.15$, ϱ_0 is the grain density (for zero porosity), ϕ_1 is the surface porosity (in percentage divided by 100), P is the lithostatic overburden pressure (in MPa), and P_c is the characteristic closure pressure of the material (in MPa). We took $\varrho_0 = 2850$ kg/m^3, $\phi_1 =$

17.5%, and $P_c = 350$ MPa from one of the solutions found by Han et al. (2014). The density profile was calculated for $P \in [0, 350]$ MPa discretised by the finite increment $\Delta P = 0.1$ MPa. The corresponding depths can be computed by the relationship of the overburden pressure with depth:

$$z = \frac{\Delta P}{g} \sum_{i=1}^{K} \frac{1}{\varrho_i}, \tag{22}$$

where $g = 1.67\ \mathrm{m/s^2}$ is the mean lunar surface gravity and K is the number of the pressure increments. Finally, the density distribution of the fourth model under consideration varies in 3D, i.e., radial, co-latitudinal, and longitudinal. It was implemented by Eq. (21) by replacing the grain density ϱ_0 with a laterally variable density grid.

The computed gravitational potential spectra from the four crustal density distributions were compared with GRAIL gravitational field model GL1500E (Konopliv et al. 2014). For consistency, SHCs of GL1500E were upward continued to the Brillouin sphere of radius $R = 1748.2$ km as they originally refer to the radius 1738 km. The comparison was performed up to d/o 1500, which is the maximum available d/o of GL1500E, in terms of the correlation γ_l, admittance Z_l, and the Bouguer correlation γ_{B_l}, each defined as:

$$\gamma_l^i = \frac{\sum_{m=0}^{l} \left(\bar{C}_{lm}^i \bar{C}_{lm}^G + \bar{S}_{lm}^i \bar{S}_{lm}^G \right)}{\sqrt{\sum_{m=0}^{l} \left[\left(\bar{C}_{lm}^i \right)^2 + \left(\bar{S}_{lm}^i \right)^2 \right]} \sqrt{\sum_{m=0}^{l} [(\bar{C}_{lm}^G)^2 + (\bar{S}_{lm}^G)^2]}}, \tag{23}$$

$$Z_l^i = \frac{\sum_{m=0}^{l} \left(\bar{C}_{lm}^i \bar{C}_{lm}^G + \bar{S}_{lm}^i \bar{S}_{lm}^G \right)}{\sum_{m=0}^{l} \left[\left(\bar{C}_{lm}^i \right)^2 + \left(\bar{S}_{lm}^i \right)^2 \right]}, \tag{24}$$

$$\gamma_{B_l}^i = \frac{\sum_{m=0}^{l} \left[\bar{C}_{lm}^i \left(\bar{C}_{lm}^G - \bar{C}_{lm}^i \right) + \bar{S}_{lm}^i \left(\bar{S}_{lm}^G - \bar{S}_{lm}^i \right) \right]}{\sqrt{\sum_{m=0}^{l} \left[\left(\bar{C}_{lm}^i \right)^2 + \left(\bar{S}_{lm}^i \right)^2 \right]} \sqrt{\sum_{m=0}^{l} \left[\left(\bar{C}_{lm}^G - \bar{C}_{lm}^i \right)^2 + \left(\bar{S}_{lm}^G - \bar{S}_{lm}^i \right)^2 \right]}}, \tag{25}$$

where the index $i \in \{1, 2, 3, 4\}$ distinguishes among the four crustal models, while the superscript G indicates the GRAIL gravitational field model GL1500E.

Preferred location of Fig. 6

The correlation spectrum γ_l between the uniform crustal model and GL1500E is depicted in Fig. 6a. It shows the highest values close to unity between ds/os 100 – 700. The correlation is reduced for ds/os less than 100 as the geophysical processes, not necessarily associated with the lunar topography, including heterogeneity in the mantle, and surface lava flows, are significant at long spatial scales. The decreasing correlation above d/o 700 is due to observation noise overwhelming the gravitational signals from GRAIL, as well as the Kaula-type constraint starting from degree 701 (Konopliv et al. 2014). Nearly indistinguishable correlations are found from the other crustal density models. This implies that the global topographic analysis of the gravitational signals are limited to ds/os 100 – 700.

In contrast, the admittance spectrum Z_l, comparing the signal powers, reveals some distinctions among the crustal models between ds/os 100 – 700 (Fig. 6b). The ideal case would give unity in correlation and admittance spectra. However, we observe a constant decrease of the admittance in the case of the uniform density model (black curve in Fig. 6b) and the laterally variable density model (blue curve in Fig. 6b). The lateral variations of the lunar crustal density affect the resulting admittance spectra only marginally, as also reported by Jansen et al. (2017). On the other hand, the radially variable density model yields almost a unity admittance spectrum between ds/os 100 – 700 (red curve in Fig. 6b) and it is slightly inclined above d/o 300. The radially variable model replicates the gravitational response to topography better than the constant and laterally variable ones. The 3D variable model yields almost identical results as the radially variable one, except for the slight shift caused by the mean density difference of 3–4%. We also note a sudden decrease of the admittances starting at degree 701 due to the Kaula-type constraint in the GL1500E model.

The Bouguer correlation spectrum γ_{B_l} provides another metric for distinguishing among the four crustal models (Fig. 6c). The ideal case would provide zeros beyond degree 100 since the crustal models are not correlated with the GRAIL data noise, if the GRAIL gravity observations are strictly interpreted as a result of the crustal density distribution. It is seen in Fig. 6c however that the minimum Bouguer correlation between the ds/os 100 – 700 (i.e., the observable crustal band) is found only for the crustal models that account for the radial density variation by compaction (green and red curves in Fig. 6c). On the contrary, the systematic decrease of the Bouguer correlation between ds/os 100–600 is found for the constant and laterally variable density models, reflecting inefficacy of these two crustal models. Beyond d/o 701, the Bouguer correlations of all crustal models decrease and approach negative unity. This is because the signal of GL1500E is significantly suppressed by the Kaula-type constraint causing each crustal model to anti-correlate with itself, see Eq. (25).

We also calculated global maps of radial gravitation, i.e., the negative gravity disturbance, generated by GL1500E and the four lunar crustal models, between ds/os 100–600 to highlight the crustal gravity changes. The global maps were evaluated on the Brillouin sphere of radius 1748.2 km with the regular equiangular step of 3/20°.

Preferred location of Fig. 7

The radial gravitation inferred by GL1500E model is depicted in Fig. 7a. The band-limited (100-600) radial gravitation values range from -335.3 mGal to 209.0 mGal, with a standard deviation of ±28.7 mGal and a mean value of 0.1 mGal. Larger variations can be seen in the lunar farside, especially in the highland areas due to more rugged topography, while the amplitudes are smaller over the low-elevated, flat lunar mare areas. This identifies the origins of high correlation between topography and gravity. Figure 7b illustrates the Bouguer radial gravitation obtained by subtracting the radial gravitation of the radially variable model from that generated by GL1500E. The values range from -42.4 mGal to 40.0 mGal with a standard deviation of ±4.5 mGal and mean of 0.03 mGal. The differences among different crustal models are as large as ~10 mGal. This demonstrates that the GRAIL gravity data are primarily explained by introducing the global rock compaction model, however there are sensible spatial variabilities in local density and the compaction model parameters.

5. Summary and conclusion

The rigorous modelling of the spherical gravitational potential spectra from the volumetric density and geometry of an attracting planetary body, herein termed the RFM technique, was presented. We started with summarising the theoretical foundations of the approach and focused on the lack of postulates that are required in other forward modelling methods. Having the mathematical apparatus in hand, we presented the numerical algorithm that makes use of the 1D discrete Fourier transform. We showed that the modelling procedures by Wieczorek and Phillips (1998) and Wieczorek (2007), also known as finite-amplitude methods, represent special simplified cases of the RFM method by imposing postulates on the volumetric density and geometry.

Our computer programs were numerically compared with the widely used (particularly in the planetary science community) routines employing finite-amplitude modelling methods. We calculated the gravitational potential spectra of the topographic masses for synthetic/simulated and realistic scenarios based on observational data of the lunar geometry and density. The numerical experiments proved correctness of the RFM algorithm. We demonstrated that the numerical calculations are manageable even for high degrees and orders (2159) of spherical harmonic expansion, and high-resolution topography and density grids by using a desktop computer. Exploitation of RFM may be advantageous over the finite-amplitude methods, which require finely-tuned input parameters. Particularly, we showed numerically that the gravitational potential spectra obtained by the finite-amplitude methods may strongly be affected by the radius of the topographic sphere, the maximum power of the topographic expansion, and, partially, by the topographic grid sampling.

Finally, we employed the RFM for modelling the gravitational field inferred by four crustal models of the Moon. These were analysed in terms of the admittance, correlation and its Bouguer counterpart, and radial gravitation with the GL1500E model from GRAIL data. Our examination confirmed that lateral variations of the crust affect the gravitational field only marginally. In contrast, the radially and spatially variable crustal models may be more realistic as they explain the inclination of the admittance and reduce the Bouguer spectra.

Acknowledgements: This research was supported partially by the Australian Government through the Australian Research Council's Discovery Projects funding scheme (project DP160104095). We thank Mark Wieczorek for sharing his own results of topography gravitational potential fields and the surface grain density, and Greg Neumann for his advice on the LOLA topography grid data. Thoughtful and constructive comments of the three anonymous reviewers are gratefully acknowledged. Thanks are also extended to the editor-in-chief Prof. Jürgen Kusche and to the responsible editor Prof. Ilias N. Tziavos for handling our manuscript.

Appendix A: Computer codes, bash scripts, and manual

The computer codes, LINUX bash scripts, and a user manual can be downloaded from the public-domain folder available at https://drive.google.com/drive/folders/0By2RsmhxzXIyLU96SzZPclVNUnM. It contains the following files:

1. **manual.pdf:** Short description of the programs, input parameters, and functionality,
2. **gravtess_uniform.f:** FORTRAN source code for calculation of the SHCs inferred by the uniform lunar crust,
3. **gravtess_lateral.f:** FORTRAN source code for calculation of the SHCs inferred by the lunar crust with laterally variable density,

4. **gravtess_radial.f:** FORTRAN source code for calculation of the SHCs inferred by the lunar crust with radially variable density,
5. **gravtess_spatial.f:** FORTRAN source code for calculation of the SHCs inferred by the lunar crust with spatially variable density,
6. **alf_sr_v121305.f:** FORTRAN source code for calculation of the integrals of the associated Legendre functions of the first kind,
7. **FFTCC.f:** FORTRAN source code necessary for the 1D discrete Fourier transform,
8. **script_uniform.sh:** Script for compiling the FORTRAN code gravtess_uniform.f90 and executing the program,
9. **script_lateral.sh:** Script for compiling the FORTRAN code gravtess_lateral.f90 and executing the program,
10. **script_radial.sh:** Script for compiling the FORTRAN code gravtess_radial.f90 and executing the program,
11. **script_spatial.sh:** Script for compiling the FORTRAN code gravtess_spatial.f90 and executing the program,
12. **depth_density_0p175_350_2850.dat:** Sample density file required by the programs gravtess_radial and gravtess_spatial,
13. **pressure_0p175_350_2850.dat:** Sample pressure file required by the program gravtess_spatial.

References

Arfken GB, Weber HJ (2005) Mathematical methods for physicists, Sixth edition. Elsevier Academic Press, New York, U.S.A., 1182 p.

Asgharzadeh MF, von Frese RRB, Kim HR, Leftwich TE, Kim JW (2007) Spherical prism gravity effects by Gauss-Legendre quadrature integration. Geophysical Journal International 169: 1-11.

Athy LF (1930) Density, porosity, and compaction of sedimentary rocks. AAPG Bulletin 14: 1-24.

Audet D, Fowler A (1992) A mathematical model for compaction in sedimentary basins. Geophysical Journal International 110: 577-590.

Balmino G (1994) Gravitational potential harmonics from the shape of an homogeneous body. Celestial Mechanics and Dynamical Astronomy 60: 331-364.

Balmino G, Lambeck K, Kaula WM (1973) A spherical harmonic analysis of the Earth's topography. Journal of Geophysical Research 78: 478-481.

Balmino G, Vales N, Bonvalot S, Briais A (2012) Spherical harmonic modelling to ultra-high degree of Bouguer and isostatic anomalies. Journal of Geodesy 86: 499-520.

Boisvert RF, Howe SE, Kahaner DK (1984) Guide to available mathematical software. NBSIR 84-2824, National Bureau of Standards, U.S. Department of Commerce, Washington DC, U.S.A., 468 p.

Casenave F, Métivier L, Pajot-Métivier G, Panet I (2016) Fast computation of general forward gravitation problems. Journal of Geodesy 90: 655-675.

Chen W, Tenzer R (2017) Moho modeling using FFT technique. Pure and Applied Geophysics 174: 1743-1757.

D'Urso MG (2013) On the evaluation of the gravity effects of polyhedral bodies and a consistent treatment of related singularities. Journal of Geodesy 87: 239-252.

Driscoll JR, Healy DM (1994) Computing Fourier transforms and convolutions on the 2-sphere. Advances in Applied Mathematics 15: 202-250.
Flury J, Rummel R (2009) On the geoid-quasigeoid separation in mountain areas. Journal of Geodesy 83: 829-847.
Fukushima T (2012a) Recursive computation of finite difference of associated Legendre functions. Journal of Geodesy 86: 745-754.
Fukushima T (2012b) Numerical computation of spherical harmonics of arbitrary degree and order by extending exponent of floating point numbers. Journal of Geodesy 86: 271-285.
Gerstl M (1980) On the recursive computation of the integrals of the associated Legendre functions. Manuscripta Geodaetica 5: 181-199.
Gleason DM (1985) Partial sums of Legendre series via Clenshaw summation. Manuscripta Geodetica 10: 115-130.
Grombein T, Luo X, Seitz K, Heck B (2014) A wavelet-based assessment of topographic-isostatic reduction for GOCE gravity gradients. Surveys in Geophysics 35: 959-982.
Grombein T, Seitz K, Heck B (2016) The Rock-Water-Ice topographic gravity field model RWI_TOPO_2015 and its comparison to a conventional Rock-Equivalent version. Surveys in Geophysics 37: 937-976.
Haagmans R, de Min E, van Gelderen M (1993) Fast evaluation of convolution integral on the sphere using 1D-FFT and a comparison with existing methods for Stokes integral. Manuscripta Geodaetica 18: 227-241.
Han S-C, Schmerr N, Neumann G, Holmes S (2014) Global characteristics of porosity and density stratification within the lunar crust from GRAIL gravity and Lunar Orbiter Laser Altimeter topography data. Geophysical Research Letters 41: 1882-1889.
Heck B, Seitz K (2007) A comparison of the tesseroid, prism and point-mass approaches for mass reductions in gravity field modelling. Journal of Geodesy 81: 121-136.
Heiskanen WA, Moritz H (1967) Physical geodesy. Freeman and Co., San Francisco, U.S.A., 364 p.
Hirt C, Kuhn M (2012) Evaluation of high-degree series expansions of the topographic potential to higher-order powers. Journal of Geophysical Research 117: B12407.
Hirt C, Kuhn M (2014) Bandlimited topographic mass distribution generates full-spectrum gravity field: Gravity forward modeling in the spectral and spatial domains revisited. Journal of Geophysical Research 119: 3646-3661.
Hirt C, Kuhn M (2017) Convergence and divergence in spherical harmonic series of the gravitational field generated by high-resolution planetary topography – a case study for the Moon. Journal of Geophysical Research, doi: 10.1002/2017JE005298.
Holmes SA, Featherstone WE (2002) A unified approach to the Clenshaw summation and the recursive computation of very high degree and order normalized associated Legendre functions. Journal of Geodesy 76: 279-299.
James PB, Zuber MT, Phillips RJ (2013) Crustal thickness and support of topography on Venus. Journal of Geophysical Research 118: 859-875.
Jansen JC, Andrews-Hanna JC, Li Y, Lucey PG, Taylor GJ, Goossens S, Lemoine FG, Mazarico E, Head III JW, Milbury C, Kiefer WS, Soderblom JM, Zuber MT (2017) Small-scale density variations in the lunar crust revealed by GRAIL. Icarus 291: 107-123.
Jekeli C (1981) The downward continuation to the Earth's surface of truncated spherical and ellipsoidal harmonic series of the gravity and height anomalies. Report No. 323, Department of Geodetic Science and Surveying, Ohio State University, Columbus, Ohio, U.S.A.

Kaula WM (1966) Theory of satellite geodesy: Applications of satellite to Geodesy. Dover Publications, Inc., New York, U.S.A., 124 p.

Kellogg OD (1929) Foundations of potential theory. Verlag von Julius Springer, Berlin, Germany, 384 p.

Konopliv AS, Park RS, Yuan D-N, Asmar SW, Watkins MM, Williams JG, Fahnestock E, Kruizinga G, Paik M, Strekalov D, Harvey N, Smith DE, Zuber MT (2013) The JPL lunar gravity field to spherical harmonic degree 660 from the GRAIL Primary Mission. Journal of Geophysical Research: Planets 118: 1415-1434.

Konopliv AS, Park RS, Yuan D-N, Asmar SW, Watkins MM, Williams JG, Fahnestock E, Kruizinga G, Paik M, Strekalov D, Harvey N, Smith DE, Zuber MT (2014) High-resolution lunar gravity fields from the GRAIL Primary and Extended Missions. Geophysical Research Letters 41: 1452-1458.

Ku CC (1977) A direct computation of gravity and magnetic anomalies caused by 2- and 3-dimensional bodies of arbitrary shape and arbitrary magnetic polarization by equivalent-point method and a simplified cubic spline. Geophysics 42: 610-622.

Kuhn M, Featherstone WE, Kirby JF (2009) Complete spherical Bouguer gravity anomalies over Australia. Australian Journal of Earth Sciences 56: 213-223.

Kuhn M, Hirt C (2016) Topographic gravitational potential up to second-order derivatives: an examination of approximation errors caused by rock-equivalent topography (RET). Journal of Geodesy 90: 883-902.

Lachapelle G (1976) A spherical harmonic expansion of the isostatic reduction potential. Bolletino di Geodesia e Scienze Affini 35: 281-299.

Lee WHK, Kaula WM (1967) A spherical harmonic analysis of the Earth's topography. Journal of Geophysical Research 72: 753-758.

Lemoine FG, Goossens S, Sabaka TJ, Nicholas JB, Mazarico E, Rowlands DD, Loomis BD, Chinn DS, Caprette DS, Neumann GA, Smith DE, Zuber MT (2013) High-degree gravity models from GRAIL primary mission data. Journal of Geophysical Research: Planets 118: 1676-1699.

Lemoine FG, Goossens S, Sabaka TJ, Nicholas JB, Mazarico E, Rowlands DD, Loomis BD, Chinn DS, Neumann GA, Smith DE, Zuber MT (2014) GRGM900C: A degree 900 lunar gravity model from GRAIL primary and extended mission data. Geophysical Research Letters 41: 3382–3389.

Li Z, Hao T, Xu Y, Xu Y (2011) An efficient and adaptive approach for modelling gravity effects in spherical coordinates. Journal of Applied Geophysics 73: 221-231.

Mazarico E, Genova A, Goosens S, Lemoine FG, Neumann GA, Zuber MT, Smith DE, Solomon SC (2014) The gravity field, orientation, and ephemeris of Mercury from MESSENGER observations after three years in orbit. Journal of Geophysical Research 119: 2417-2436.

Moritz H (1989) Advanced physical geodesy, 2nd Edition. Herbert Wichmann Verlag, Karlsruhe, Germany, 500 p.

Nagy D, Papp G, Benedek J (2000) The gravitational potential and its derivatives for the prism. Journal of Geodesy 74: 552-560.

Neumann GA, Zuber MT, Wieczorek MA, McGovern PJ, Lemoine FG, Smith DE (2004) Crustal structure of Mars from gravity and topography. Journal of Geophysical Research 109: E08002.

Novák P, Grafarend EW (2005) Ellipsoidal representation of the topographical potential and its vertical gradient. Journal of Geodesy 78: 691-706.

Novák P, Grafarend EW (2006) The effect of topographical and atmospheric masses on space borne gravimetric and gradiometric data. Studia Geophysica et Geodaetica 50: 549-582.

Paul MK (1978) Recurrence relations for integrals of associated Legendre functions. Bulletin Géodésique 52: 177-190.

Pavlis NK, Rapp RH (1990) The development of an isostatic gravitational model to degree 360 and its use in global gravity modelling. Geophysical Journal International 100: 369-378.

Pohánka V (1988) Optimum expression for computation of the gravity field of a homogeneous polyhedral body. Geophysical Prospecting 36: 733-751.

Rexer M, Hirt C, Claessens S, Tenzer R (2016) Layer-based modelling of the Earth's gravitational potential up to 10-km scale in spherical harmonics in spherical and ellipsoidal approximation. Surveys in Geophysics 37: 1035-1074.

Root BC, Novák P, Dirkx D, Kaban M, van der Wal W, Vermeersen LLA (2016) On a spectral method for forward gravity field modelling. Journal of Geodynamics 97: 22-30.

Roussel C, Verdun J, Cali J, Masson F (2015) Complete gravity field of an ellipsoidal prism by Gauss-Legendre quadrature. Geophysical Journal International 203: 2220-2236.

Rummel R, Rapp RH, Sünkel H, Tscherning CC (1988) Comparisons of global topographic/isostatic models to the Earth's observed gravity field. Report No. 388, Department of Geodetic Science and Surveying, Ohio State University, Columbus, Ohio, U.S.A.

Sansò F, Sideris MG (2013) Geoid determination: theory and methods. Springer-Verlag, Berlin Heidelberg, Germany, 734 p.

Sjöberg LE (2006) A refined conversion from normal height to orthometric height. Studia Geophysica et Geodaetica 50: 595-606.

Smith DE, Zuber MT, Neumann GA, Lemoine FG, Mazarico E, Torrence MH, McGarry JF, Rowlands DD, Head III JW, Duxbury TH, Aharonson O, Lucey PG, Robinson MS, Barnouin OS, Cavanaugh JF, Sun X, Liiva P, Mao D-D, Smith JC, Bartels AE (2010) Initial observations from the Lunar Orbiter Laser Altimeter (LOLA). Geophysical Research Letters 37: L18204.

Sun W, Sjöberg LE (2001) Convergence and optimal truncation of binomial expansions used in isostatic compensations and terrain corrections. Journal of Geodesy 74: 627-636.

Tenzer R, Hirt C, Claessens S, Novák P (2015) Spatial and spectral representations of the geoid-to-quasigeoid correction. Surveys in Geophysics 36: 627-658.

Tenzer R, Hirt C, Novák P, Pitoňák M, Šprlák M (2016) Contribution of mass density heterogeneities to the quasigeoid-to-geoid separation. Journal of Geodesy 90: 65-80.

Tenzer R, Novák P, Gladkikh V (2012) The bathymetric stripping corrections to gravity field quantities for a depth-dependent model of the seawater density. Marine Geodesy 35: 1-23.

Torge W, Müller J (2012) Geodesy, 4th Edition. De Gruyter Inc., Berlin, Boston, 433 p.

Turcotte DL, Schubert G (2014) Geodynamics, 3rd Edition. Cambridge University Press, New York, U.S.A., 626 p.

Uieda L, Barbosa VCF, Braitenberg C (2016) Tesseroids: Forward-modelling gravitational field in spherical coordinates. Geophysics 81: 41-48.

Vajda P, Ellmann A, Meurers B, Vaníček P, Novák P, Tenzer R (2008) Global ellipsoid-referenced topographic, bathymetric and stripping corrections to gravity disturbance. Studia Geophysica et Geodaetica 52: 19-34.

Vaníček P, Huang J, Novák P, Pagiatakis S, Véronneau M, Martinec Z, Featherstone WE (1999) Determination of the boundary values for the Stokes-Helmert problem. Journal of Geodesy 73: 180-192.

Wang YM, Yang X (2013) On the spherical and spheroidal harmonic expansion of the gravitational potential of the topographic masses. Journal of Geodesy 87: 909-921.

Werner RA (2017) The solid angle hidden in polyhedron gravitation formulations. Journal of Geodesy 91: 307-328.

Werner RA, Scheeres DJ (1997) Exterior gravitation of a polyhedron derived and compared with harmonic and mascon gravitation representations of asteroid 4769 Castalia. Celestial Mechanics and Dynamical Astronomy 65: 313-344.

Wessel P, Smith WHF, Scharroo R, Luis JF, Wobbe F (2013) Generic Mapping Tools: Improved version released, EOS - Transactions of the AGU 94(45): 409-410, doi: 10.1002/2013EO450001.

Wieczorek MA (2007) Gravity and topography of the terrestrial planets. Treatise on Geophysics, Vol. 10, Elsevier, Amsterdam, the Netherlands, pp. 165-206.

Wieczorek MA (2015) Gravity and topography of the terrestrial planets. Treatise on Geophysics, 2nd edition, Vol. 10, Elsevier, Oxford, U.K., pp. 153-193.

Wieczorek MA, Meschede M, Oshchepkov I (2015) SHTOOLS - Tools for working with spherical harmonics (v3.1). Zenodo. doi:10.5281/zenodo.20920.

Wieczorek MA, Neumann GA, Nimmo F, Kiefer WS, Taylor GJ, Melosh HJ, Phillips RJ, Solomon SC, Andrews-Hanna JC, Asmar SW, Konopliv AS, Lemoine FG, Smith DE, Watkins MM, Williams JG, Zuber MT (2013) The crust of the Moon as seen by GRAIL. Science 339: 671-675.

Wieczorek MA, Phillips RJ (1998) Potential anomalies on a sphere: applications to the thickness of the lunar crust. Journal of Geophysical Research 103: 1715-1724.

Wild-Pfeiffer F (2008) A comparison of different mass elements for use in gravity gradiometry. Journal of Geodesy 82: 637-653.

Zuber MT, Smith DE, Lehman DH, Hoffman TL, Asmar SW, Watkins MM (2013) Gravity Recovery and Interior Laboratory (GRAIL): Mapping the Lunar Interior from Crust to Core. Space Science Reviews 178: 3-24.

Figure captions:

Fig. 1: Square-root of degree variances calculated from the SHC differences (dimensionless) between the analytical solution for the spherical shell of constant density, see Eq. (20), and the RFM (black) and the method by WP98 up to maximum powers of the topographic expansion $n_{max} = 1$ (red), 10 (blue), and 20 (green).

Fig. 2: Square root of degree variances from the SHCs (dimensionless) calculated by RFM. The gravitational potential spectra were inferred by the topographic masses of the Moon with the constant density $\varrho = 2550$ kg/m^3 and referred to four different spheres of radii 1728.2 km (red), 1737.4 km (blue), 1738.0 km (black), and the Brillouin 1748.2 km (green).

Fig. 3: Square root of degree variances from the SHCs (dimensionless) calculated by the forward modelling method by WP98. The gravitational potential spectra were determined by exploiting the LOLA topography discretised with the steps $\Delta\theta' = \Delta\lambda' = 1/28°$ and a constant density $\varrho = 2550$ kg/m^3. The various radii D of the topographic sphere are 1737.4 km (black), 1728.2 km (red) and 1748.2 km (blue). Curve styles resolve different maximum powers of the topographic expansion $n_{max} = 1$ (dotted), 10 (dashed), and 20 (solid). All spectra refer to the Brillouin sphere of radius $R = 1748.2$ km.

Fig. 4: Same as in Fig. 3, but the curve styles distinguish individual powers of the topography being $n = 1$ (dotted), 10 (dashed), and 20 (solid). The gravitational potential spectra refer to the corresponding topographic spheres.

Fig. 5: Square root of degree variances calculated from the SHCs and from coefficient differences (dimensionless). Spectra of the reference SHCs as determined by the RFM with the LOLA topography discretised with steps $\Delta\theta' = \Delta\lambda' = 1/14°$ (black). Spectra of the differences between the reference SHCs and those computed by the RFM with the LOLA topography with equiangular sampling of 1/28° (green). Spectra of the differences between the reference SHCs and those computed by the approach by WP98 with the LOLA topography with equiangular sampling of 1/28° (red) and 1/56° (blue). All spectra refer to the Brillouin sphere of radius $R = 1748.2$ km.

Fig. 6: Spectral characteristics of the gravitational potential spectra as determined by the lunar crustal models: **a)** the correlation of Eq. (23), **b)** the admittance of Eq. (24), and **c)** the Bouguer correlation of Eq. (25). The four crustal models of the bulk density are uniform (black), laterally variable (blue), radially variable (red) and variable in 3D (green).

Fig. 7: Lunar maps of: **a)** the radial gravitation generated from the GL1500E model and **b)** the Bouguer radial gravitation. The Bouguer radial gravitation was obtained by subtracting the values implied by the radially variable crustal model from those of GL1500E. Left hemispheres depict the nearside; right hemispheres depict the farside. Orthographic projection with centres located at $\theta = 0°, \lambda = 0°$ (left hemispheres) and $\theta = 0°, \lambda = -180°$ (right hemispheres). Meridians and parallels are spaced at 30° intervals.

Figure 1

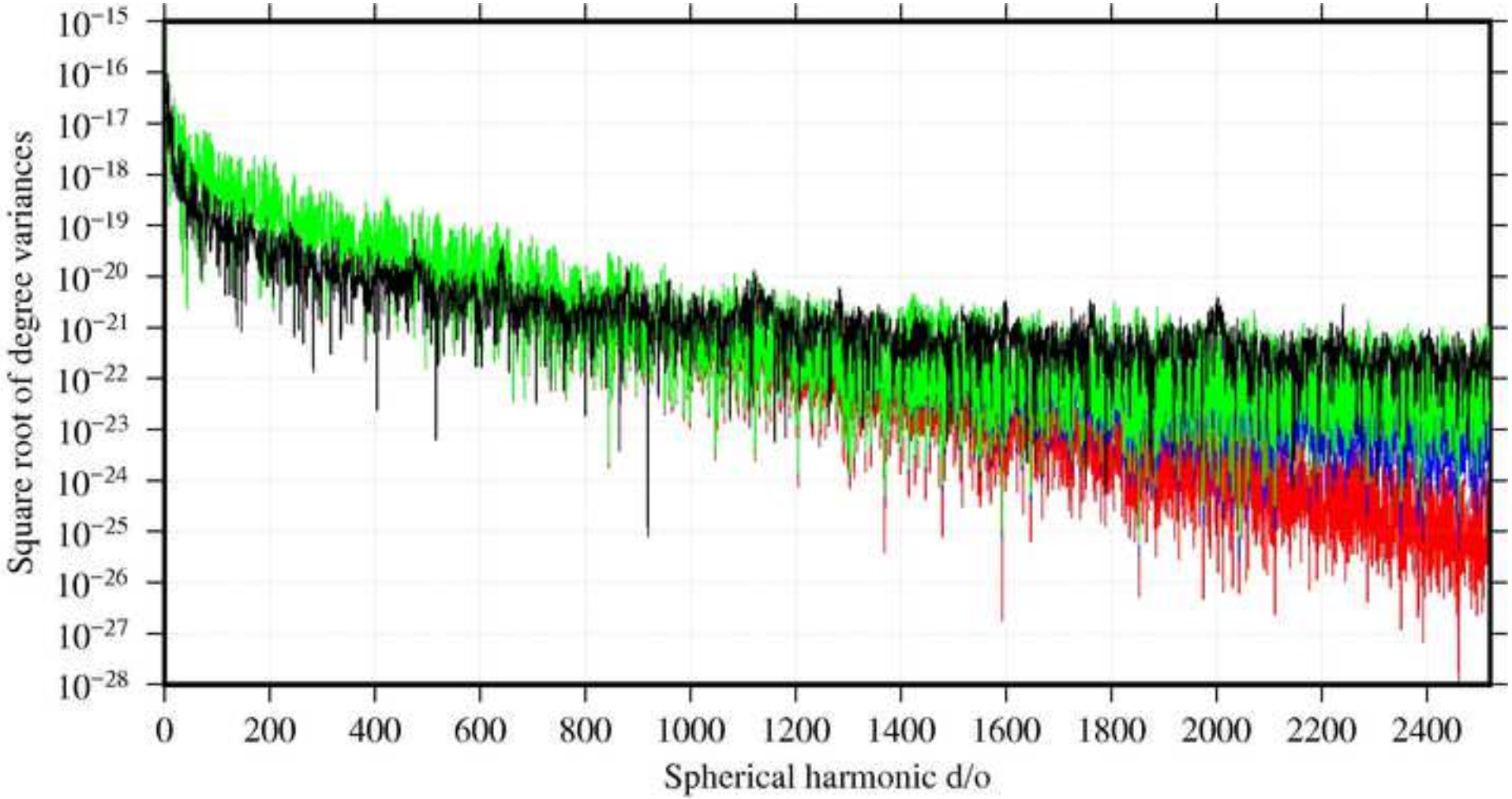
Square root of degree variances
10^{-15}
10^{-16}
10^{-17}
10^{-18}
10^{-19}
10^{-20}
10^{-21}
10^{-22}
10^{-23}
10^{-24}
10^{-25}
10^{-26}
10^{-27}
10^{-28}
0
200
400
600
800
1000
1200
1400
1600
1800
2000
2200
2400
Spherical harmonic d/o

Figure 2

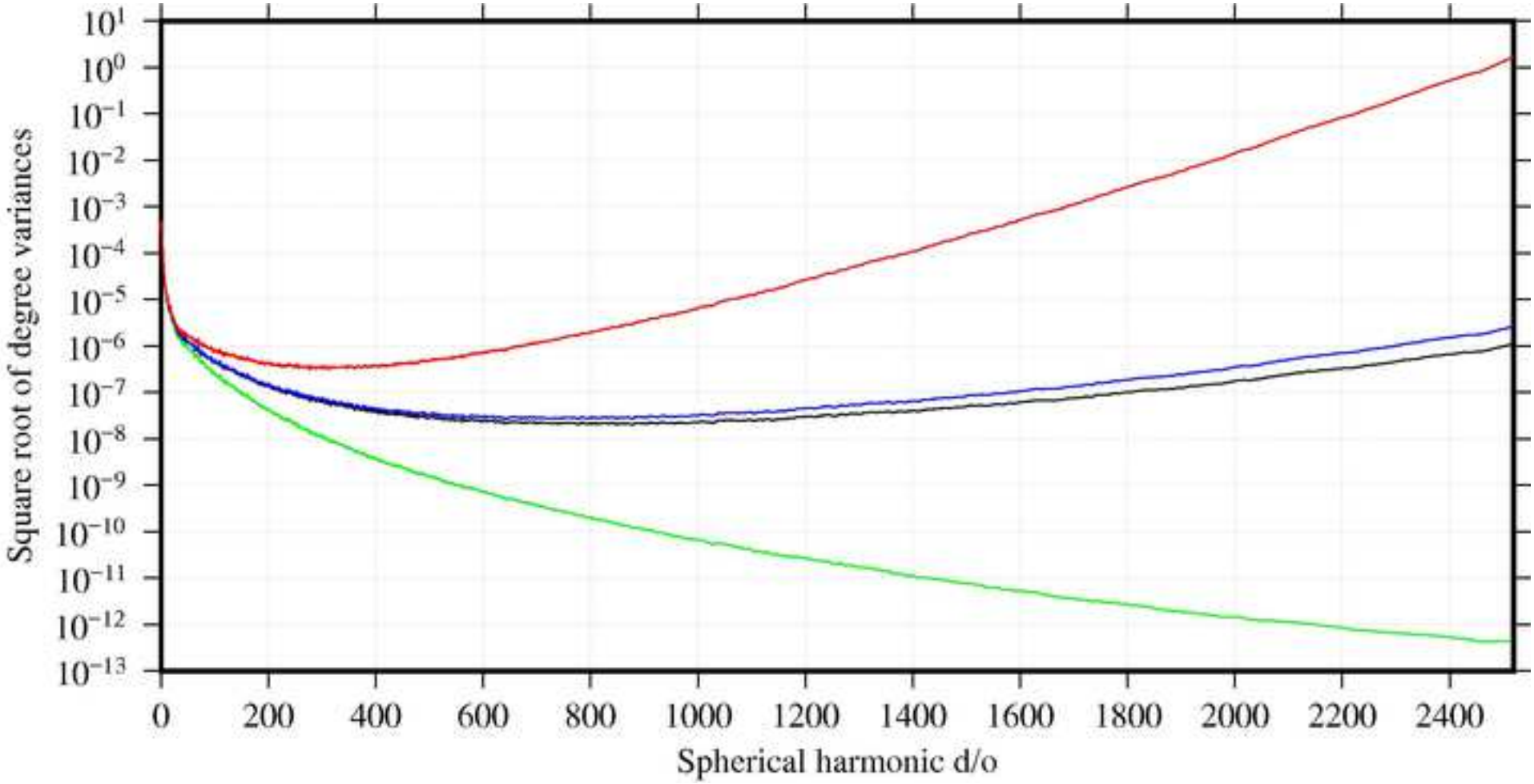
Square root of degree variances
10^{1}
10^{0}
10^{-1}
10^{-2}
10^{-3}
10^{-4}
10^{-5}
10^{-6}
10^{-7}
10^{-8}
10^{-9}
10^{-10}
10^{-11}
10^{-12}
10^{-13}
0
200
400
600
800
1000
1200
1400
1600
1800
2000
2200
2400
Spherical harmonic d/o

Figure 3

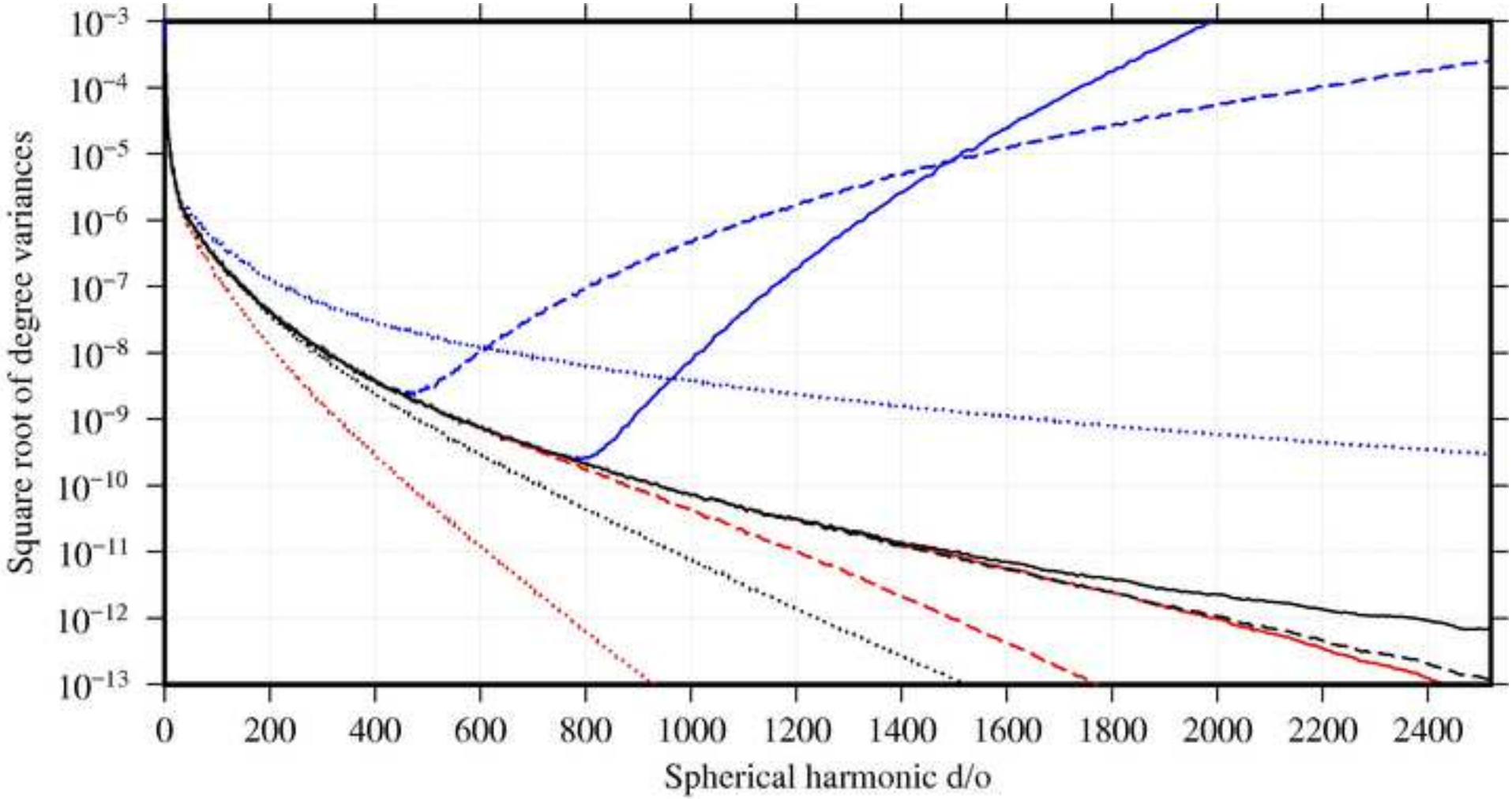
Square root of degree variances
10^{-3}
10^{-4}
10^{-5}
10^{-6}
10^{-7}
10^{-8}
10^{-9}
10^{-10}
10^{-11}
10^{-12}
10^{-13}
0
200
400
600
800
1000
1200
1400
1600
1800
2000
2200
2400
Spherical harmonic d/o

Figure 4

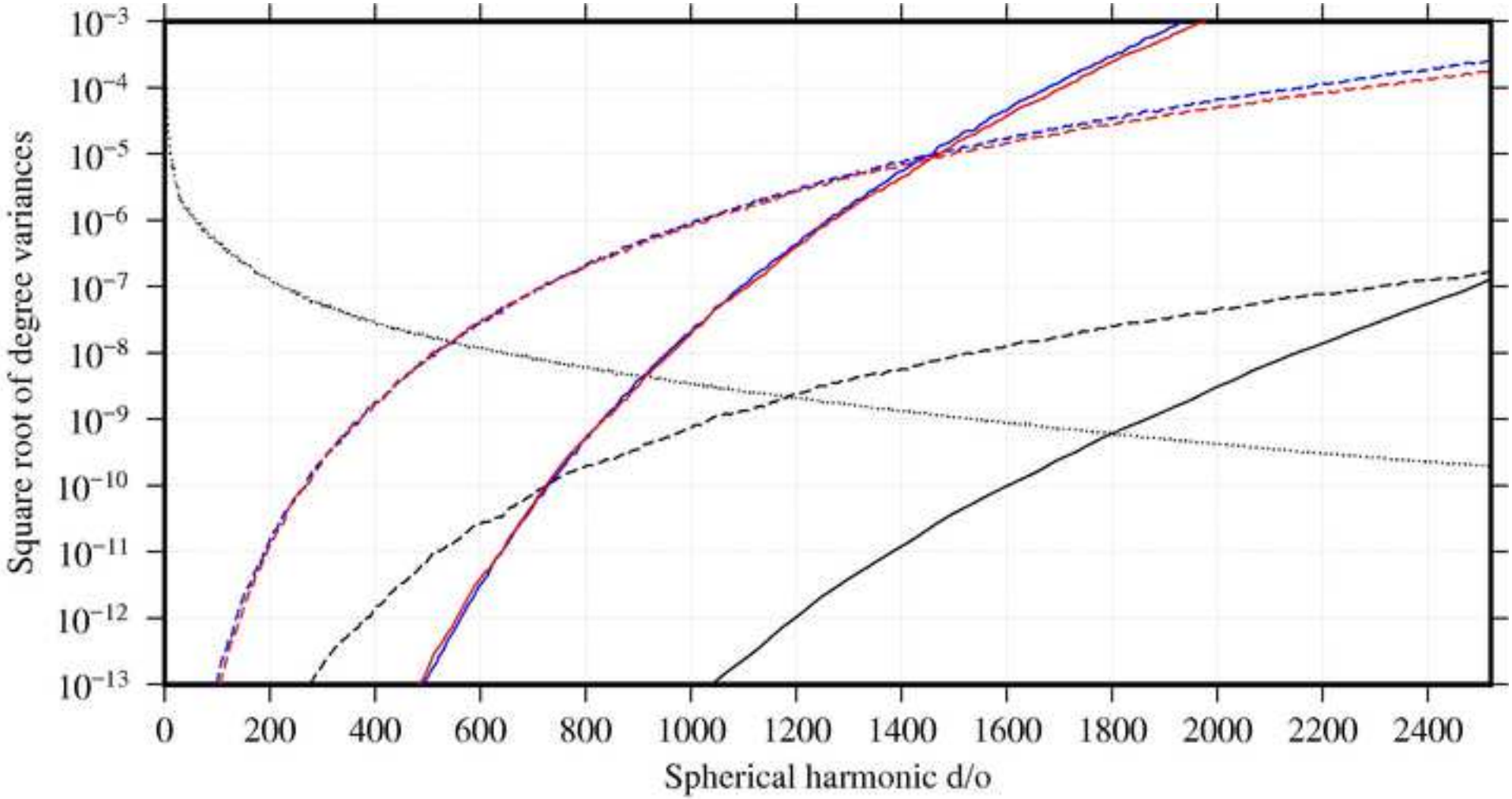
Square root of degree variances
10^{-3}
10^{-4}
10^{-5}
10^{-6}
10^{-7}
10^{-8}
10^{-9}
10^{-10}
10^{-11}
10^{-12}
10^{-13}
0
200
400
600
800
1000
1200
1400
1600
1800
2000
2200
2400
Spherical harmonic d/o

Figure 5

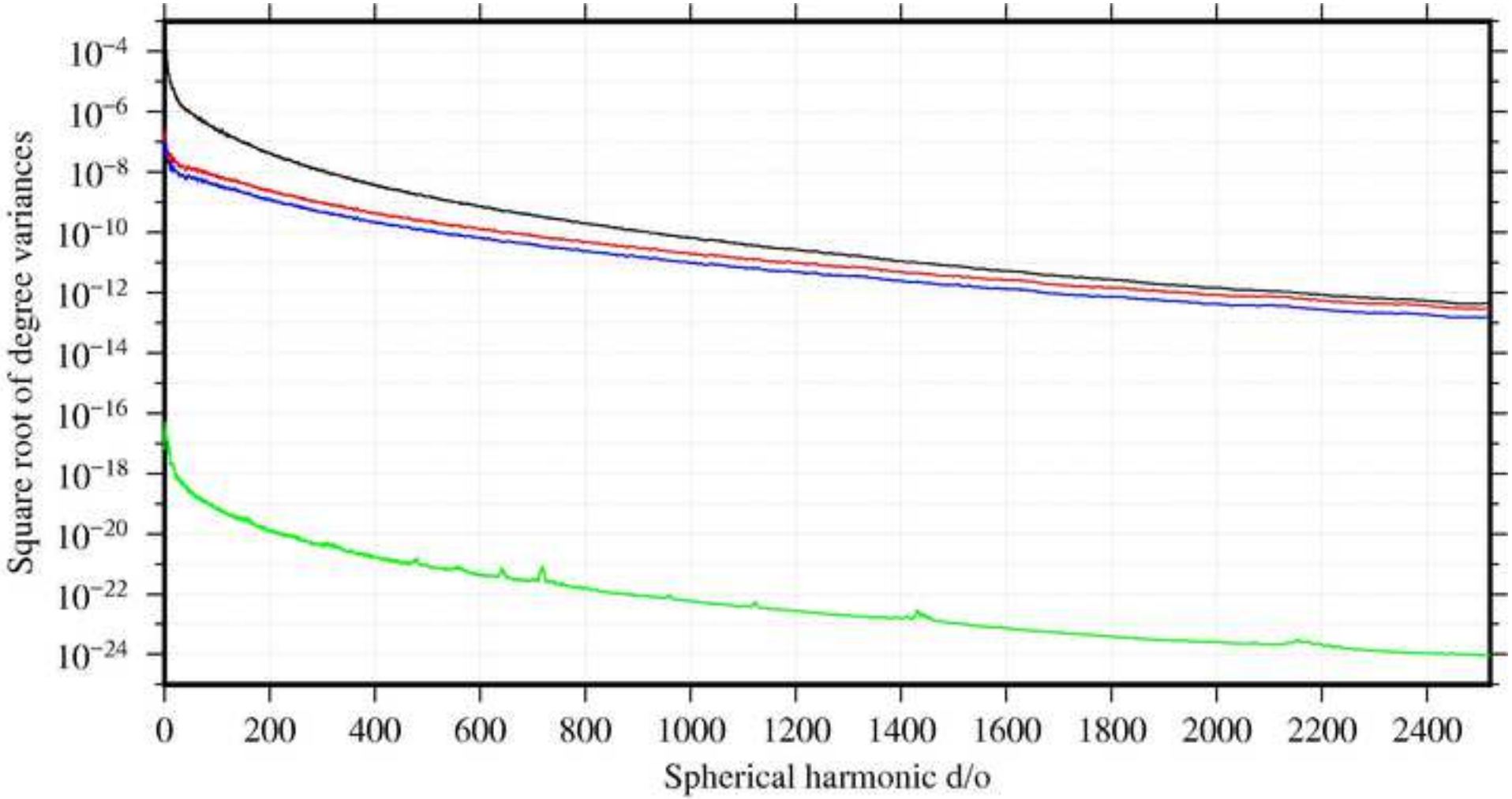
Square root of degree variances
10^{-4}
10^{-6}
10^{-8}
10^{-10}
10^{-12}
10^{-14}
10^{-16}
10^{-18}
10^{-20}
10^{-22}
10^{-24}
0
200
400
600
800
1000
1200
1400
1600
1800
2000
2200
2400
Spherical harmonic d/o

Figure 6

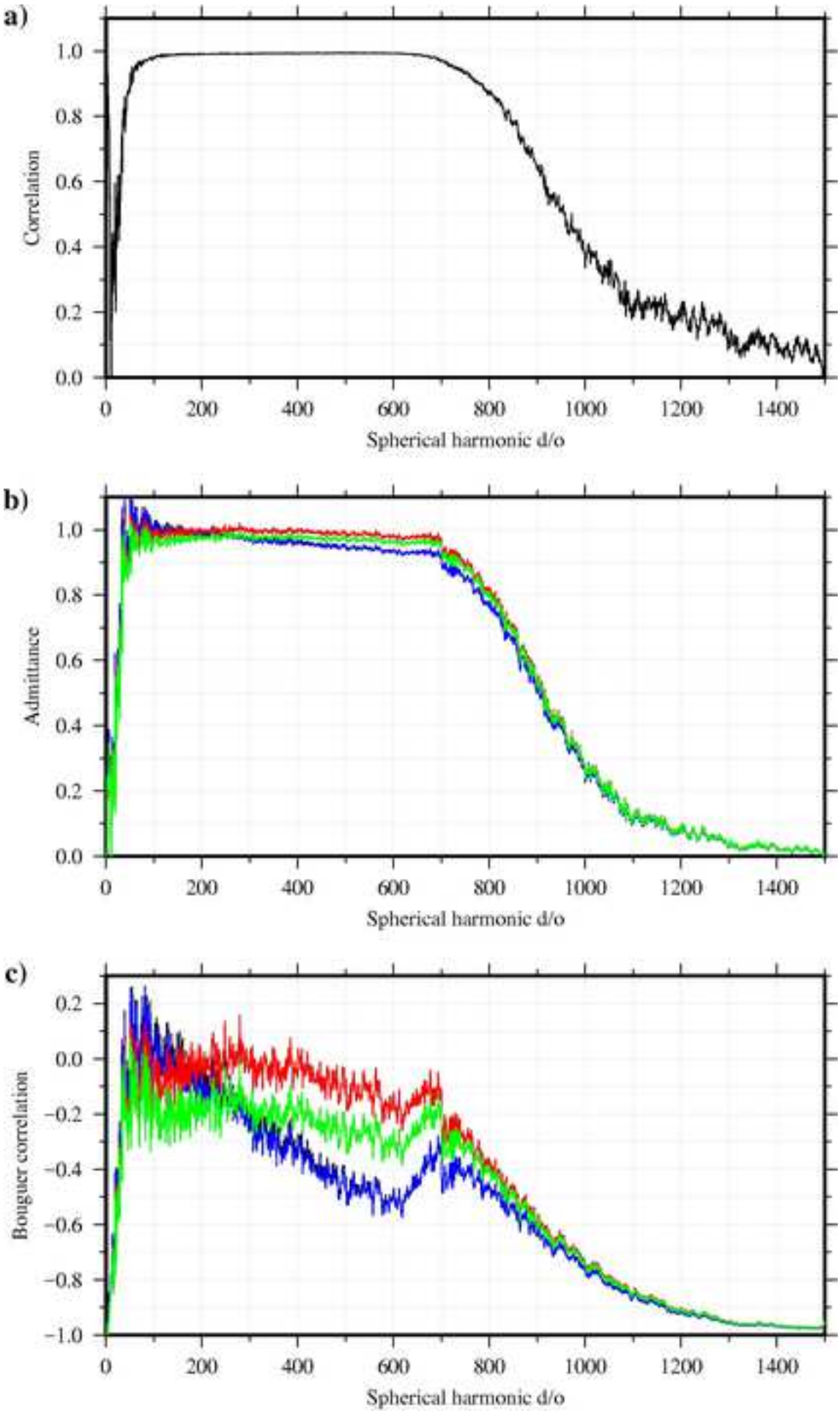
a)
Correlation
1.0
0.8
0.6
0.4
0.2
0.0
0
200
400
600
800
1000
1200
1400
Spherical harmonic d/o
b)
Admittance
1.0
0.8
0.6
0.4
0.2
0.0
0
200
400
600
800
1000
1200
1400
Spherical harmonic d/o
c)
Bouguer correlation
0.2
0.0
−0.2
−0.4
−0.6
−0.8
−1.0
0
200
400
600
800
1000
1200
1400
Spherical harmonic d/o

Figure 7